



CHALMERS
UNIVERSITY OF TECHNOLOGY

Temperature-dependent structural and magnetic properties of R₂MMnO₆ double perovskites (R=Dy, Gd; M=Ni, Co)

Downloaded from: <https://research.chalmers.se>, 2026-05-09 21:43 UTC

Citation for the original published paper (version of record):

Ivanov, S., Andersson, M., Cedervall, J. et al (2018). Temperature-dependent structural and magnetic properties of R₂MMnO₆ double perovskites (R=Dy, Gd; M=Ni, Co). *Journal of Materials Science: Materials in Electronics*, 29(21): 18581-18592.
<http://dx.doi.org/10.1007/s10854-018-9976-1>

N.B. When citing this work, cite the original published paper.



Temperature-dependent structural and magnetic properties of R_2MMnO_6 double perovskites ($R = \text{Dy, Gd}$; $M = \text{Ni, Co}$)

S. A. Ivanov^{1,2} · M. S. Andersson^{2,3} · J. Cedervall⁴ · E. Lewin⁴ · M. Sahlberg⁴ · G. V. Bazuev⁵ · P. Nordblad² · R. Mathieu² 

Received: 19 June 2018 / Accepted: 31 August 2018 / Published online: 4 September 2018
© The Author(s) 2018

Abstract

The structural and magnetic properties of the $\text{Dy}_2\text{CoMnO}_6$, $\text{Dy}_2\text{NiMnO}_6$ and $\text{Gd}_2\text{CoMnO}_6$ double perovskites are investigated using X-ray powder diffraction and squid magnetometry. The materials adopt an orthorhombic structure (space group $Pnma$) with disordered $\text{Co}(\text{Ni})/\text{Mn}$ cations, and exhibit ferrimagnetic transitions near $T_C \sim 85, 95,$ and 115 K respectively. T_C was found to monotonously depend on the orthorhombic distortion $(a-c)/(a+c)$ of the compounds. The crystal structure of the compounds was investigated as a function of temperature (16–1100 K range), evidencing changes in the BO_6 octahedron near T_C . The magnetic entropy changes are estimated for comparison of the magnetocaloric properties to those from literature.

1 Introduction

The $A_2B'B''O_6$ double perovskites (A : rare earth; B' and B'' : magnetic cations such as Mn, Fe, Co, or Ni) display cross-correlated structural, electronic and magnetic properties owing to the strong coupling of spin, charge, orbital and lattice degrees of freedom in these materials [1–4]. As a result, these transition metal oxides exhibit rich electronic phase diagrams, suggesting novel functionalities and industrial relevance. For example, some of these double perovskites display magnetoresistive [5] or magnetoelectric properties [6], making them relevant for spintronic applications [7]. Recently, also magnetocaloric properties of these materials have become of interest [8–10]. Large magnetic entropy changes have indeed been observed near room temperature

in some manganites at their ferromagnetic phase transition and at lower temperatures down to liquid helium temperatures, in materials with specific interplay of $4f$ and $3d$ magnetic moments [11–19]. Several studies show that the change of magnetic entropy near room temperature in $\text{La}_{1-x}\text{A}_x\text{MnO}_3$ ($A = \text{Ca, Sr, Ba}$) is close to, or in some cases even higher than that of pure gadolinium [18, 20–23]. The Curie temperature and other magnetic properties of these manganese oxides result from a complex interplay of various factors such as $\text{Mn}^{3+}/\text{Mn}^{4+}$ cation ratio, the average A -site cation radius and size mismatch, the oxygen stoichiometry, charge ordering etc. [24–26]. In $\text{Gd}_2\text{CoMnO}_6$, entropy changes related both to the ferrimagnetic ordering of Co/Mn cations near 110 K and at lower temperatures ($T \sim 10$ K) due to the presence of large Gd magnetic moments and their coupling to the $3d$ moments were recently reported [11, 12, 27, 28].

In recent years, rare earth double perovskites R_2MMnO_6 (M being Ni or Co) have attracted widespread attention due to their rich physical properties, showing a complicated interplay between electric and magnetic properties [1–10, 28–31]. However, in contrast to the extensively investigated $\text{La}_2\text{CoMnO}_6$ compound, less consideration has been given to other perovskite manganites such as R_2MMnO_6 ($R = \text{Dy}$ and Gd) [32–38]. In the $R_2\text{CoMnO}_6$ family, a change in the size of the rare-earth ion can induce significant alterations in the Co-O-Mn bond angle and bond length, which significantly modifies the superexchange interaction and consequently affects their electronic and magnetic ground states [3, 4, 8]. Among the rare earth elements, Gd and Dy are interesting

✉ R. Mathieu
roland.mathieu@angstrom.uu.se

¹ Center of Materials Science, Karpov Institute of Physical Chemistry, Vorontsovo Pole 10, Moscow, Russia 105064

² Department of Engineering Sciences, Uppsala University, Box 534, 751 21 Uppsala, Sweden

³ Department of Chemistry and Chemical Engineering, Chalmers University of Technology, 412 96 Gothenburg, Sweden

⁴ Department of Chemistry - Ångström Laboratory, Uppsala University, Box 538, 751 21 Uppsala, Sweden

⁵ Institute of Solid State Chemistry, Ural Branch of the Russian Academy of Sciences, Ekaterinburg, Russia 620990

as A-cation due to their large magnetic moment [28, 31–35]. A few studies have attempted to correlate the changes in structure with the variations in the nature of magnetic ordering in these compounds [1, 2, 4, 8]. However, no systematic investigation of the evolution of the crystal structure from high temperatures to low temperatures through the magnetic phase transitions have been reported. The symmetry of the crystal structure of these perovskites has been a matter of discussion in several investigations [2, 4, 39–42]. Two different space groups have been proposed: orthorhombic $Pnma$ and monoclinic $P2_1/n$. This disagreement about the proper space group of these systems calls for further investigations of the entire family, including ordered and disordered models.

This investigation concerns structural and magnetic properties of the double perovskites Dy_2CoMnO_6 , Dy_2NiMnO_6 and Gd_2CoMnO_6 . The novelty of this study is a detailed structural characterization over a wide temperature range, 16–1100 K, correlated with the magnetic transitions and the evolution of the magnetic properties from 200 K down to 10 K.

2 Experimental

2.1 Synthesis

The samples of R_2MMnO_6 ($R = Dy$ or Gd , $M = Co$ or Ni) were obtained by the solid-phase reaction method from the simple oxides Dy_2O_3 , Gd_2O_3 , Co_3O_4 , NiO and Mn_2O_3 , which had purities greater than 99.95% of the main substance. Stoichiometric mixtures of reagent-grade precursor materials were first weighed, thoroughly mixed and ball milled for several hours, pressed under the pressure of 3000 kg/cm^2 , and sintered in air at temperatures 950, 1100, 1250 and 1350 °C in electrical furnace with intermediate grinding after each 12 h, until the X-ray powder diffraction (XRPD) showed the expected patterns without impurity lines. The overall duration of sintering was 48 h. Upon the final annealing, the specimens were cooled inside the furnace to room temperature. The mixtures were weighed before and after heat treatment to determine possible cation losses due to evaporation. In all cases, the weight difference was negligible ($< 0.01\%$). Leaching with warm dilute nitric acid was used to eliminate small amount of unreacted dysprosium oxide.

2.2 X-ray powder diffraction

The phase purity of the powder samples was checked from XRPD patterns obtained with a D-5000 diffractometer using $Cu K\alpha$ radiation. The ceramic samples were crushed into powder in an agate mortar and suspended in ethanol. A Si

substrate was covered with several drops of the resulting suspension, leaving randomly oriented crystallites after drying. The room temperature XRPD data for Rietveld analysis were collected on Bruker D8 Advance diffractometer (Gemonochromatized $Cu K\alpha_1$ radiation, Bragg–Brentano geometry, a Lynx-eye position sensitive detector, DIFFRACT plus software) in the 2θ range $10\text{--}152^\circ$ with a step size of 0.02° (counting time was 15 s per step). The slit system was selected to ensure that the X-ray beam was completely within the sample for all 2θ angles. The X-ray diffraction measurements at variable temperature in the temperature range 16–1073 K were carried out using the same setup and an Anton Paar XRK 900 chamber (300–1073 K) or an Oxford Phenix cryostat (16–300 K). The temperature dependent measurements were performed using a 2θ -range of $20\text{--}90^\circ$ with a step size of 0.017° . The duration of diffraction scan at fixed temperature was around 12 h. Structural refinements were performed using the Rietveld method as implemented in the FULLPROF software suite [43]. The difference between the high and low temperature setups was taken into account using a normalization of the lattice parameters to the room temperature values adding a reference material NIST SRM 660b LaB_6 .

2.3 Chemical composition

The chemical composition of the prepared ceramic samples was analyzed by energy-dispersive spectroscopy (EDS) using a Philips Epsilon3 spectrometer. The analyses confirm the presence of the constituent elements ($Dy(Gd)$, $Ni(Co)$, Mn). For each sample, the composition was derived from the average of five consecutive measurements (see Table 1).

2.4 XPS

Photoelectron spectroscopy was conducted using an Ulvac-Phi Quantera II spectrometer, which employs monochromatic $Al K\alpha$ radiation (1486.7 eV). For the present experiments the analysis spot was set to a diameter of 100 μm , and an electron take-off angle of 45° was used. The energy scale was calibrated against reference samples of Au, Ag and Cu, according to ISO 15472 standard [44]. Measurements were conducted on solid pieces of the perovskites directly from synthesis. To remove adsorbed surface contaminants (but not affect the sample), and increase the sample signal, a presputter step was employed using a 200 eV Ar^+ ionbeam for 0.2 min. As the samples are electrically insulating, they were measured under constant charge neutralization with an electron flood gun and low energy (10 eV) Ar^+ ions, as described in reference [45]. This procedure guarantees stable measurement conditions, but not an exact binding energy—a charge reference is needed. However, due to the presputter step the commonly used charge reference adventitious carbon

Table 1 Cation concentrations estimated from EDS analysis compared to nominal ones (weight percentages)

R_2MMnO_6	R	Exp. (wt%)	Theo. (wt%)	Actual formula
Dy_2NiMnO_6	Dy	74.01 (4)	74.09	$Dy_{1.98(1)}Ni_{1.01(1)}Mn_{1.01(1)}O_6$
	Ni	13.42 (4)	13.38	
	Mn	12.57 (4)	12.53	
Dy_2CoMnO_6	Dy	73.97 (4)	74.05	$Dy_{1.99(1)}Co_{1.01(1)}Mn_{1.00(1)}O_6$
	Co	13.48 (5)	13.43	
	Mn	12.55 (4)	12.52	
Gd_2CoMnO_6	Gd	73.45 (4)	73.41	$Gd_{2.01(1)}Co_{1.00(1)}Mn_{0.99(1)}O_6$
	Co	13.69 (5)	13.76	
	Mn	12.86 (4)	12.83	

could not be used, instead all spectra have been adjusted using O 1s at 530.0 eV as charge reference. Core level spectra for all elements in the samples were collected for all samples.

2.5 Magnetization

Temperature and magnetic field dependent magnetization was measured using a Quantum Design MPMS SQUID magnetometer. The temperature dependent magnetization was recorded using zero field cooled, $M_{ZFC}(T)$, and field cooled, $M_{FC}(T)$, protocols in the temperature interval 10 and 200 K and at two different magnetic fields: $H=0.8$ kA/m and $H=800$ kA/m. Magnetization as a function of applied magnetic field was measured between ± 4000 kA/m at a few selected temperatures.

3 Results

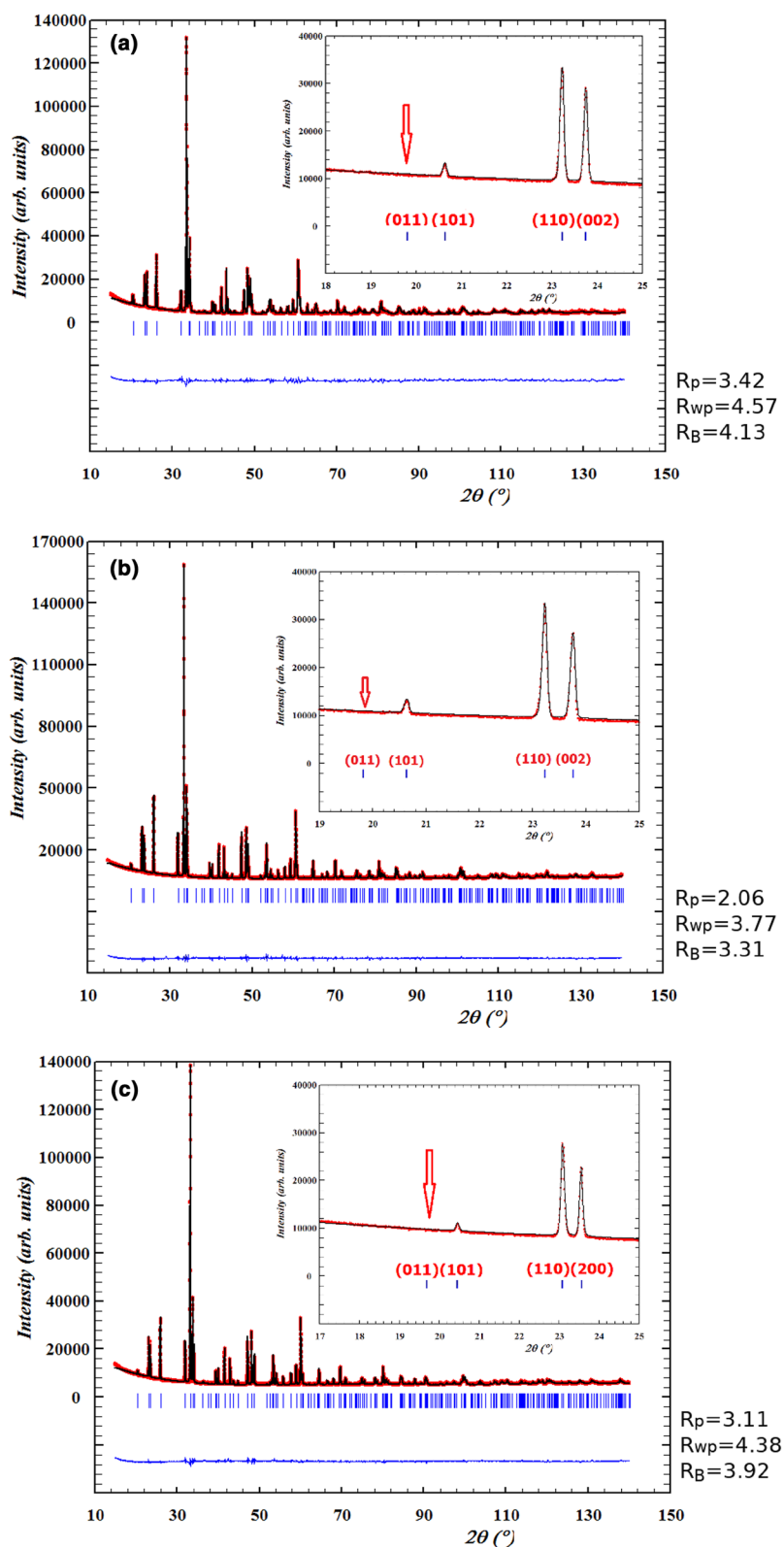
According to the elemental analyses the cation composition of the samples are quite close to the expected ratios and permit to conclude that the sample stoichiometry is the nominal. However, a minute deficit on the A -site may possibly be discerned in the case of the Dy samples (Table 1). The crystallographic characterization of the samples was performed by X-ray powder diffraction analysis at room temperature. Figure 1a–c shows the XRPD patterns of the Gd_2CoMnO_6 (GCMO), Dy_2CoMnO_6 (DCMO) and Dy_2NiMnO_6 (DNMO) powders measured at 295 K. The Rietveld analyses of these diffractograms were conducted using the FULLPROF software considering the different combinations of valence states for the B -cations (M^{2+}/Mn^{4+} and M^{3+}/Mn^{3+} ; $M=Co, Ni$) using orthorhombic ($Pnma$) and monoclinic ($P2_1/n$) structure models. The orthorhombic unit cell with $a \sim \sqrt{2}a_p$, $b \sim 2a_p$ and $c \sim \sqrt{2}a_p$ was successfully applied for the indexation of the XRPD pattern and the $Pnma$ space group was found to best describe the crystal structure of the samples. The lattice parameters of the tested compounds are in reasonable agreement with those reported earlier in [31, 34,

36–38] and theoretically calculated by the SPuDS program [46]. There is, however, some disagreement with the cell parameters reported in Ref [38]. This difference in lattice parameters could be explained by different sample preparation methods.

The R cations have coordination number 8 instead of 12 in these compounds. The reduced coordination number of the A -type cations is due to large octahedral tilting which implies that some nearest neighbor anions fall outside of the first coordination sphere about the A -cation. It has been proposed [47] that any anion more than 3.00 Å away from the A -cation of double perovskites may be considered to be outside the coordination sphere.

The temperature dependence of the lattice parameters is shown in Figs. 2, 3, and 4. An anomaly in the temperature dependence of the lattice parameters can be discerned in all samples around T_C (~ 100 K), in spite of relatively large temperature steps in between points. Below T_C , the lattice parameters are weakly temperature dependent. At high temperatures, a normal thermal expansion of the lattice parameters is observed and no phase transformations were found in any of the investigated compounds. In the orthorhombic unit cell there are the three crystallographically independent bond lengths ($B-O1(4c)$, $B-O2(8d)$ and $B-O2(8d)$) and two bond angles ($B-O1-B$, $B-O2-B$) bond angles. The temperature dependencies of the $B-O$ bond lengths and $B-O-B$ bond angles are presented in Fig. 5. There are abrupt changes in both the bond lengths and the bond angles for all samples near T_C . The temperature dependence of the first $B-O2$ bond exhibits an inverse behavior as compared to the other $B-O2$ bond. The $B-O2-B$ bond angles are larger as compared to the $B-O1-B$ angles for all compositions and temperatures, but both values are substantially smaller than 180°. According to the Goodenough-Kanamori rules [48, 49], this indicates moderately strong ferro- or antiferromagnetic interaction between the magnetic moments of the metal cations. In the case of orthorhombic $Pnma$ structure a cooperative rotation of the BO_6 octahedra remarkably reduces the $B-O-B$ bond angle from 180°. Ordering of Co^{2+} and Mn^{4+} cations on the other hand leads to monoclinic $P2_1/n$ structure

Fig. 1 Room temperature XRPD patterns of **a** $\text{Dy}_2\text{NiMnO}_6$, **b** $\text{Dy}_2\text{CoMnO}_6$, and **c** $\text{Gd}_2\text{CoMnO}_6$. Observed (black dots) and calculated (red solid line) intensities, and their difference (blue line at the bottom) are plotted. The blue tick marks indicate the positions of the allowed Bragg reflections. The insets show the low-angle region in more details. (Color figure online)



and strong 180° -superexchange interactions giving rise to high magnetic transition temperatures.

From the individual cation–anion distances, the valences of the cations were estimated via bond valence calculations [50]. The calculated values of the cation sites slightly differ

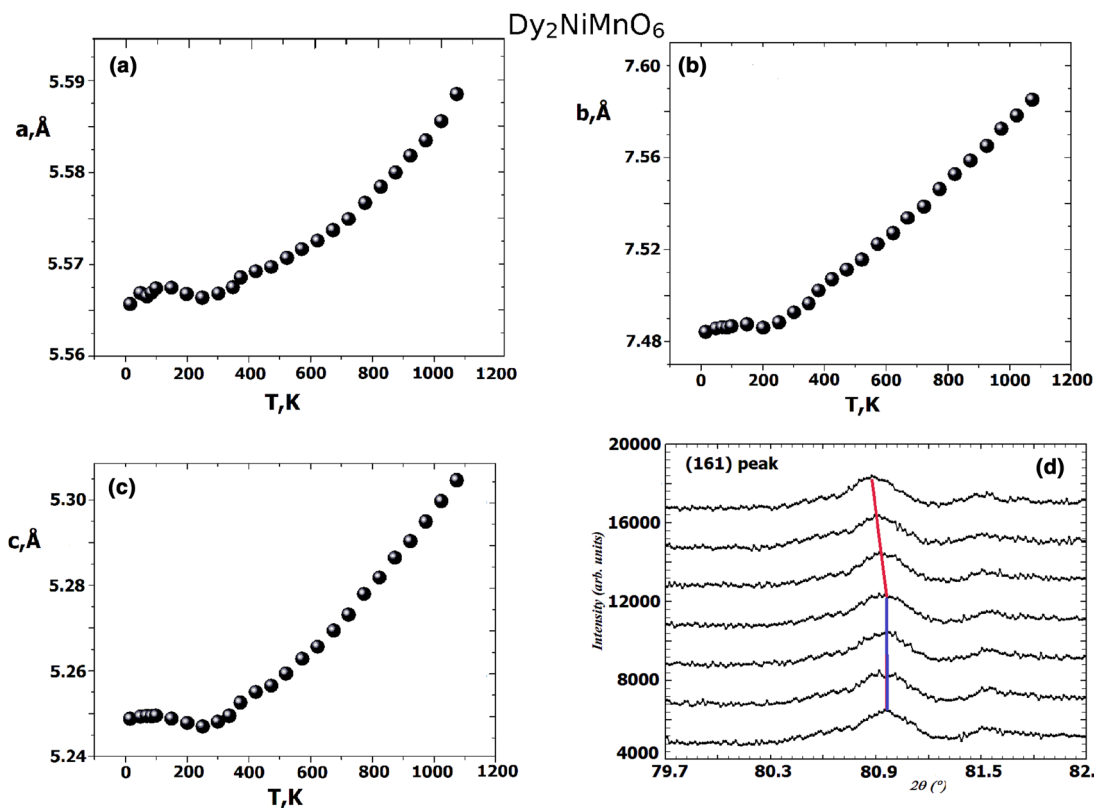


Fig. 2 a–c Temperature dependence of the lattice parameters for Dy₂NiMnO₆ extracted from the XRPD patterns. The temperature evolution of the (161) reflection is shown in (d)

from the expected valences of the cations in these compounds (see Table 2). The results suggest that the *M* and Mn cations exist in mixed (M^{2+} , M^{3+} , Mn^{3+} , Mn^{4+}) valences, and that the compounds may not be oxygen stoichiometric. A majority of the Ni and Mn cations existing as Ni^{3+} and Mn^{3+} in the Ni compound, and Co and Mn existing mainly as Co^{2+} and Mn^{3+} in the two Co compounds. Metal core level photoelectron spectra for all three samples are shown in Fig. 6. A comparison of the relative shifts gives some hints, but a conclusive determination of the metal valence states was not possible with the present data. An increase in the binding energy for the Mn 2p peak (Fig. 6a) for the Ni-containing sample, compared to the Co-containing samples, indicate that the average Mn valence is higher for the Ni-containing sample [51]. There is also a similar relative shift for the Dy 4d (Fig. 6d) and Dy 3d (not shown) peaks, also indicating a higher average valence for Dy in Ni-containing sample. Furthermore, a difference in the shake-up (+6.4 eV from main peak) of Co 2p_{3/2} (Fig. 6(c)) indicates a slight difference in average Co valence between samples with Dy and Gd, respectively. The Dy-containing sample has a larger shake-up peak, which is consistent with more Co^{2+} in the sample [51], i.e. a slightly lower average valence than the Gd-containing sample.

Figure 7 presents data from the low magnetic field ($H = 0.8$ kA/m) $M_{ZFC}(T)$ and $M_{FC}(T)$ measurements (a–c) and high field ($H = 800$ kA/m) $M_{FC}(T)$ measurements (d–f). The temperature dependence of the magnetization suggests a ferrimagnetic arrangement of the 3d magnetic moments of the compounds. From the low field measurements the transition temperature T_C was estimated for the three samples; $T_C = 95$ K for Dy₂NiMnO₆, $T_C = 85$ K for Dy₂CoMnO₆, and $T_C = 115$ K for Gd₂CoMnO₆. These transition temperatures agree well with what has earlier been reported in the literature; Dy₂NiMnO₆ 93 K and 97 K [32, 52], Dy₂CoMnO₆ 85 K and 90 K [22, 28], and Gd₂CoMnO₆ ~ 112 K and 117 K [11, 28]. For Dy₂NiMnO₆ and Gd₂CoMnO₆ a decrease in magnetization is seen below 50 K indicating that the RE moments couple antiferromagnetically to the spontaneous moment of the magnetically ordered 3d ions. In Fig. 8, which shows the data from magnetization as a function of temperature measurements in a high applied magnetic field, the low temperature contribution of the rare earth moments can be clearly seen. The different behavior observed for the three compounds indicates that they have different coupling strength and sign between the rare earth moments and the ordered 3d moments. From the high field data ($\mu_0 H = 1$ T) the magnetic entropy change

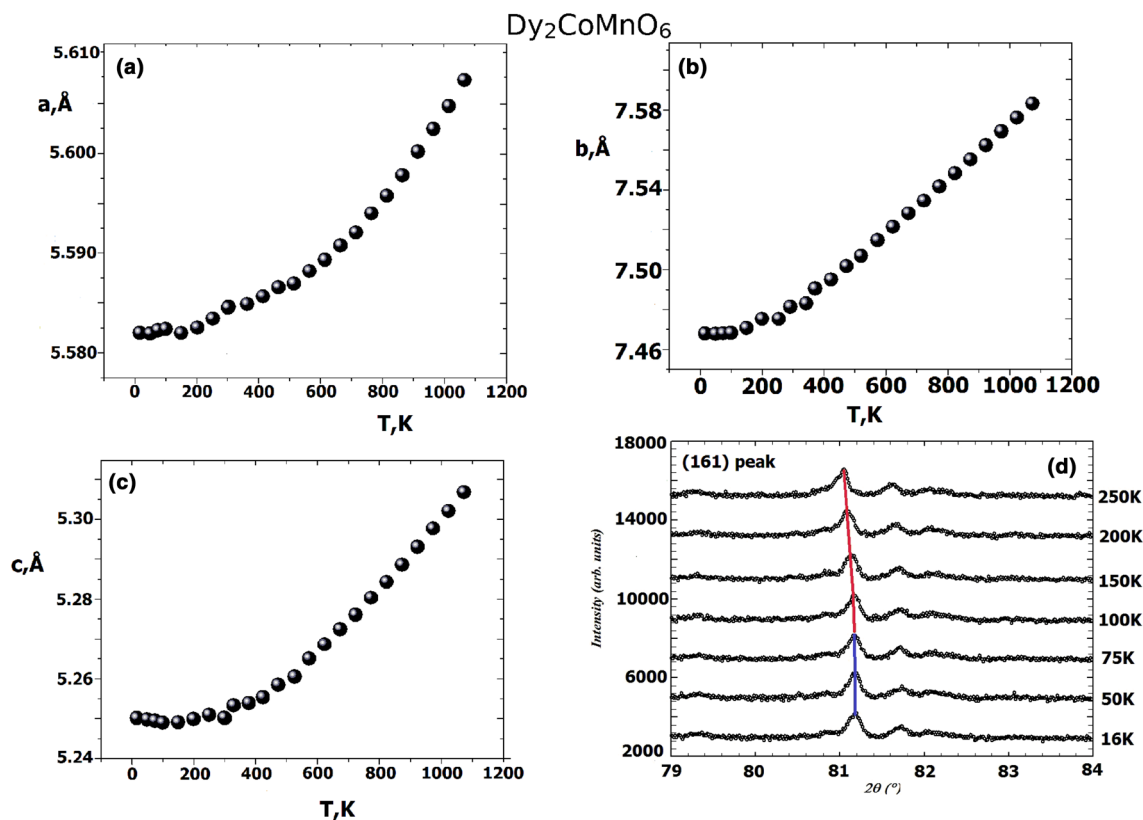


Fig. 3 a–c Temperature dependence of the lattice parameters for Dy₂CoMnO₆ extracted from the XRPD patterns. The temperature evolution of the (161) reflection is shown in d

can be estimated using the formula $\Delta S \approx dM/dT \times \mu_0 H$ [53], which yielded $-\Delta S(T \approx T_C) \approx 0.45, 0.30$ and 0.55 J/kgK for Dy₂NiMnO₆, Dy₂CoMnO₆ and Gd₂CoMnO₆ respectively, in agreement with the results of recent studies [11, 17, 31, 32, 35]. As seen from the insets of Fig. 8, the entropy change at low temperatures is much larger than that around T_C , reflecting the contribution of the 4f moments of Dy and Gd to the magnetic and magnetocaloric properties of the systems [12, 17]. Data for measurements of the magnetization as a function of applied magnetic field for two temperatures (10 and 70 K) are presented in Fig. 9. The curves at 70 K all exhibits characteristic ferrimagnetic behavior, with a linear increase of the magnetization at higher fields where the spontaneous magnetization has been aligned with the applied field. The data at 10 K shows that none of the compounds saturate at an applied field of 5 T. The coercivity of the three samples differ, with Dy₂NiMnO₆ having a small coercivity, while Dy₂CoMnO₆ and Gd₂CoMnO₆ has a moderate and a large coercivity, respectively. This is reflected in the difference between the ZFC and FC magnetization curves presented in Fig. 7.

4 Discussion

The structural and magnetic properties of the perovskite $R_2\text{CoMnO}_6$ are strongly influenced by the synthesis method as well as by doping [4, 8, 10, 54–56]. In fact, the perfectly ordered double perovskite is difficult to obtain due to the ease at which formation of anti-site disorder occurs. The distribution of CoO₆ and MnO₆ octahedra is influenced by the annealing process and atmosphere [54–57]. Very often, the monoclinic structure is easier to form by slow-cooling while orthorhombic structure will appear under quenched conditions [2, 47, 57].

Neighbor pairs of Co and Mn atoms turn into Co²⁺ and Mn⁴⁺ in the case of structural order at B-sublattice, whereas the fraction of Co³⁺/Mn³⁺ (high spin) in $R_2\text{CoMnO}_6$ increases as the disorder of Co and Mn ions is enhanced [58]. Factors influencing the extent of cation order in double perovskites are charge differences between the B-cations, their differences in ionic radii, the polarization of certain cations and synthetic conditions [59].

Because the symmetry of the crystal structure of $R_2\text{CoMnO}_6$ was a matter of discussion in several works [2, 4, 8], an important part of the motivation for this research was to clarify the possibility of B-site ordering. The difference

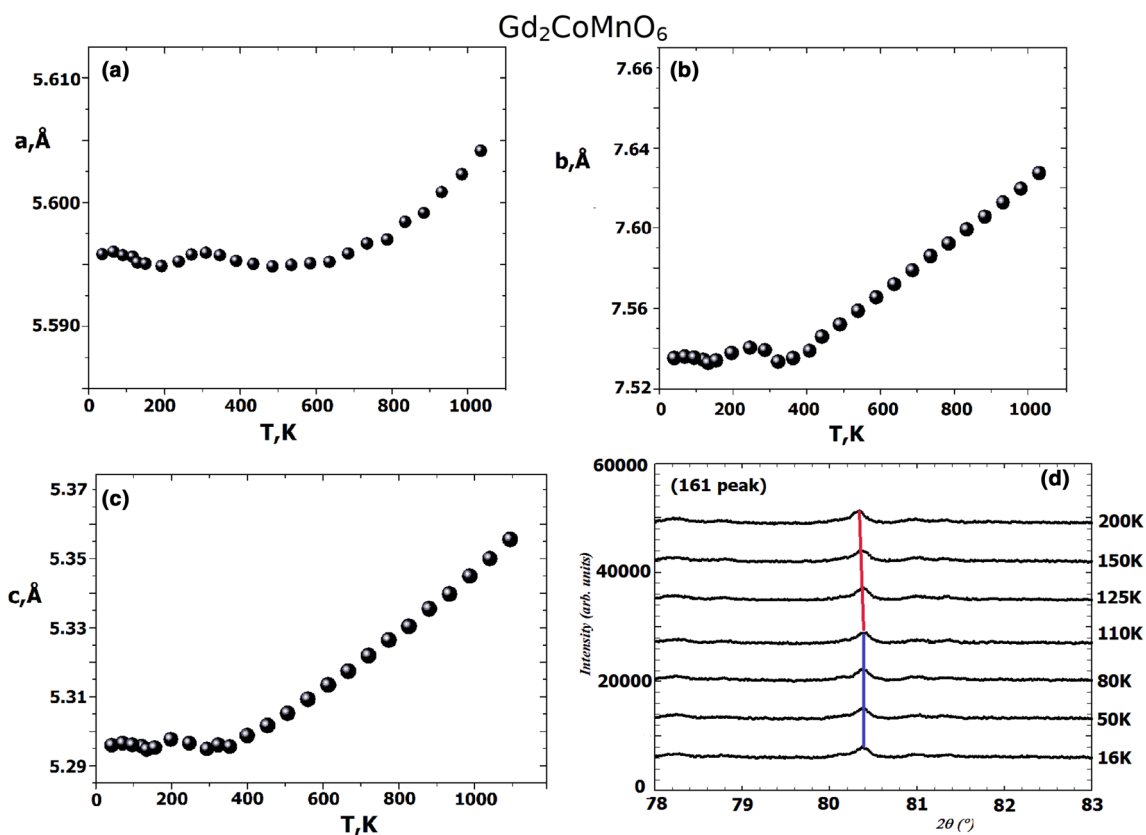


Fig. 4 a–c Temperature dependence of the lattice parameters for $\text{Gd}_2\text{CoMnO}_6$ extracted from the XRPD patterns. The temperature evolution of the (161) reflection is shown in d

in charge between B' and B'' cations is the most important factor influencing cation ordering [59]. If the difference in assigned oxidation state is two or less, several ordering arrangements are possible, dominated by completely disordered and partially ordered arrangements. If the difference is greater than two, highly ordered compounds are generally observed. The second most influential factor is the cation size difference of the B -cations [59]. In general, larger differences in ionic radii of B -site cations correlate to higher degrees of cation ordering.

For the investigated perovskites there are two space groups that correspond to the $a^+b^-b^-$ tilt system: orthorhombic $Pnma$ and monoclinic $P2_1/n$. $Pnma$ is assigned to disordered and simple perovskites, whereas $P2_1/n$ is assigned to compounds with partial or complete rock-salt order of the B -site cations. The diffraction patterns for compounds crystallizing in these space groups are very similar. In principle the monoclinic distortion would be detectable either through splitting of peaks as β angle is not 90° , or by the observation of additional diffraction peaks. Peaks with $0kl$ indices are observed in $P2_1/n$, but their appearance in $Pnma$ is limited by the $k+l=2n$ reflection condition. For example, the (011)

reflection is indicative of cation ordering and will not be observed if the compound has $Pnma$ symmetry. The XRPD patterns for all compounds examined here were without any (011) reflections (see insets in Fig. 1), and thus the $Pnma$ symmetry was used to refine each data set. The final fits after Rietveld refinement are shown in Fig. 1. The quality of refinements in space group $P2_1/n$ were not significantly better than that of refinements in the disordered orthorhombic model and the deviation of the refined value of β from 90° was not significant (in the frame of standard deviation). However, since the potential ordering is between Co (Ni) and Mn cations differing by only 2 (or 3) electrons, the amplitude of an ordering peak in XRPD pattern is expected to be very weak.

These materials have been investigated previously but the reported structural models show discrepancies e.g. in the B -O bond distances derived from different diffraction techniques [1, 2, 4]. It has often been possible to only obtain accurate positions for the rare earth ions which could be due to both the low scattering power of oxygen compared to the lanthanide and the inability of the XRPD technique to distinguish between the two different B ions due to their similar scattering factors.

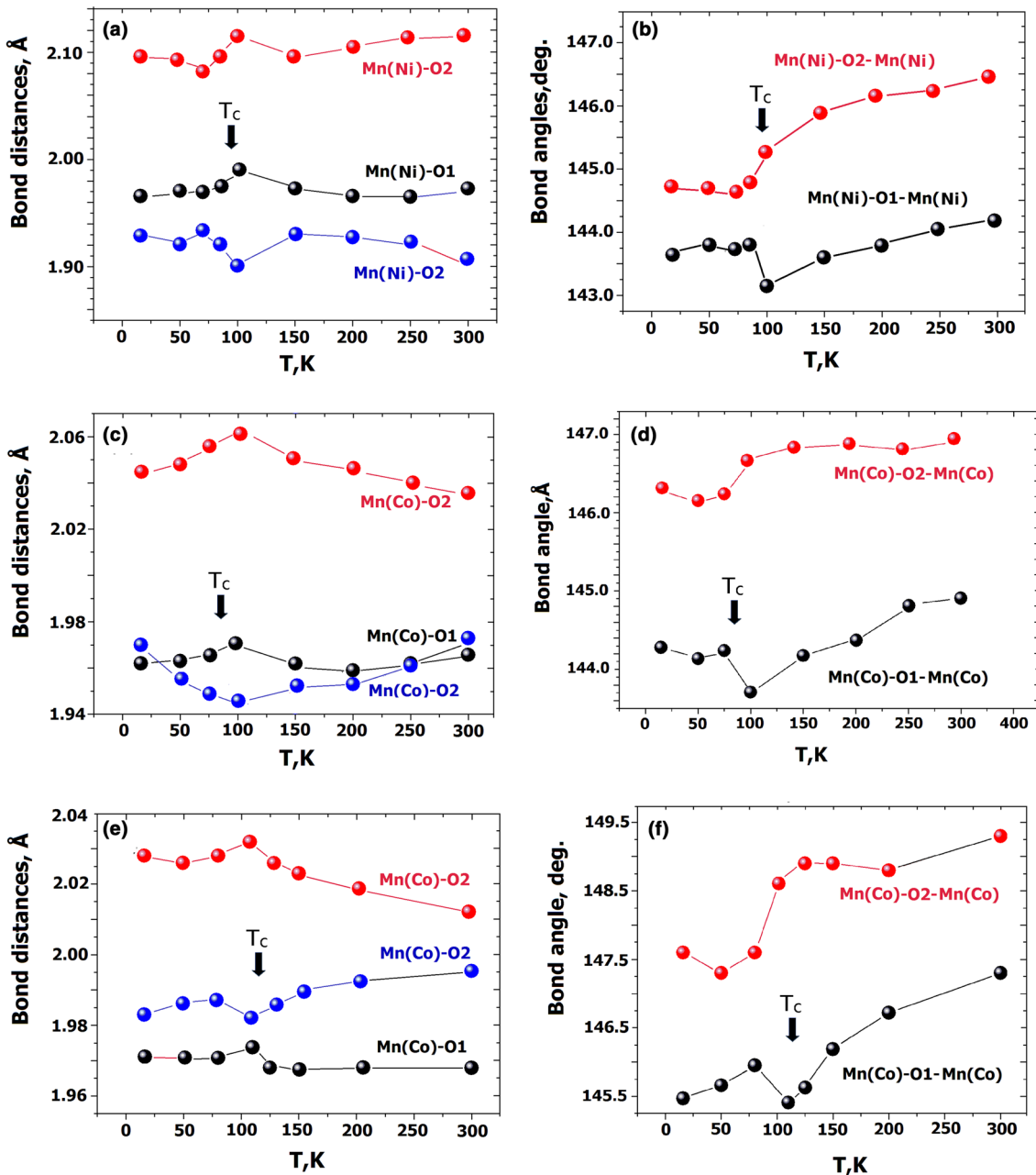


Fig. 5 Temperature dependence of the bond angles (left) and angles (right) of $\text{Dy}_2\text{NiMnO}_6$ (a, b), $\text{Dy}_2\text{CoMnO}_6$ (c, d), and $\text{Gd}_2\text{CoMnO}_6$ (e, f). The T_c values determined from magnetization measurements are indicated with arrows

Table 2 Cations valences estimated from BVS calculations

$R_2\text{MMnO}_6$	R	M	Mn
$\text{Dy}_2\text{NiMnO}_6$	2.78(3)	2.73(2)	3.34(3)
$\text{Dy}_2\text{CoMnO}_6$	2.87(3)	2.31(2)	3.20(3)
$\text{Gd}_2\text{CoMnO}_6$	2.86(3)	2.35(2)	3.28(3)

The M vs. H curves measured at 70 K show ferrimagnetic behavior with rather weak net moments and characteristic linear increase of the magnetization at higher fields for all samples. The ferrimagnetic transition temperature does not vary monotonously with the $B-O-B$ bond angles nor $B-O$ bond lengths. However, T_c decreases nearly linearly as the orthorhombic distortion $(a-c)/(a+c)$ increases, as illustrated in Fig. 10. The M vs. H curves at 10 K reflect the combined effect of the ferrimagnetically ordered 3d moments and the

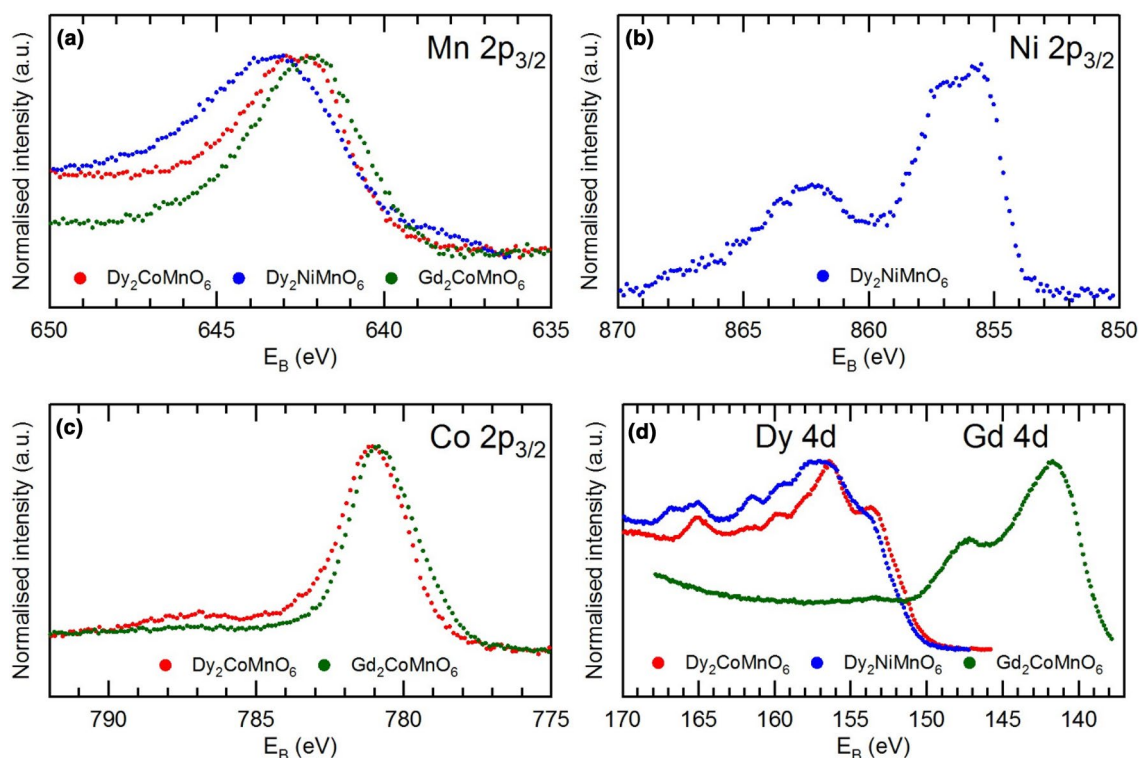


Fig. 6 XPS spectra of **a** the three samples (Mn 2p binding energy region). **b** $\text{Dy}_2\text{NiMnO}_6$ (Ni 2p); **c** $\text{Dy}_2\text{CoMnO}_6$, and $\text{Gd}_2\text{CoMnO}_6$ (Co 2p); **d** the three samples (Dy 4d–Gd 4d)

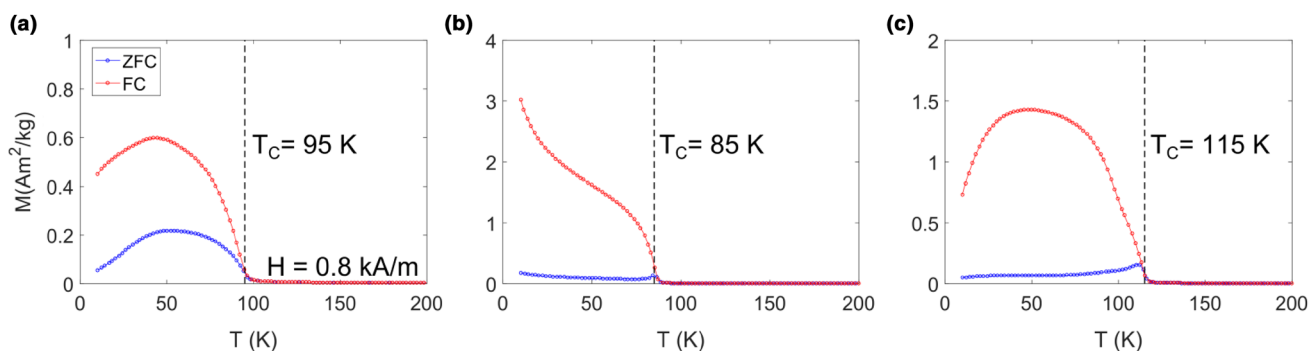


Fig. 7 Temperature dependence of the ZFC/FC magnetization for **a** $\text{Dy}_2\text{NiMnO}_6$, **b** $\text{Dy}_2\text{CoMnO}_6$, and **c** $\text{Gd}_2\text{CoMnO}_6$, recorded in $H=0.8$ kA/m

alignment of the 4f moments. The nonlinear behavior at all field strengths indicates significant coupling to the 3d system in all three systems. The measured coercive fields extracted from Fig. 9 are 40 mT (DNMO), 160 mT (DCMO) and 340 mT (GCMO) at $T=5$ K (6, 77, and 160 mT, respectively, at 70 K). The different coercive fields of the three compounds are directly reflected in the low field M vs. T experiments, where the two Co based samples have coercivities much larger than 800 A/m (1 mT) already just below T_C as is reflected in the behavior of the gap between the ZFC and FC curves and the peaked ZFC

curve at T_C . The difference in coercivity between the Ni and the Co containing compounds relates directly to the much lower single ion anisotropy of the Ni compared to the Co ions.

The temperature dependence of the magnetic entropy ΔS derived from the high field (1 T) M vs. T curves is plotted in the insets of Fig. 8 for all samples. The values of ΔS near T_C are of similar magnitude for all three samples and quite modest due to the compensated low value of the spontaneous magnetization of ferrimagnets and the second order nature of the transition. The alignment of the large 4f moments

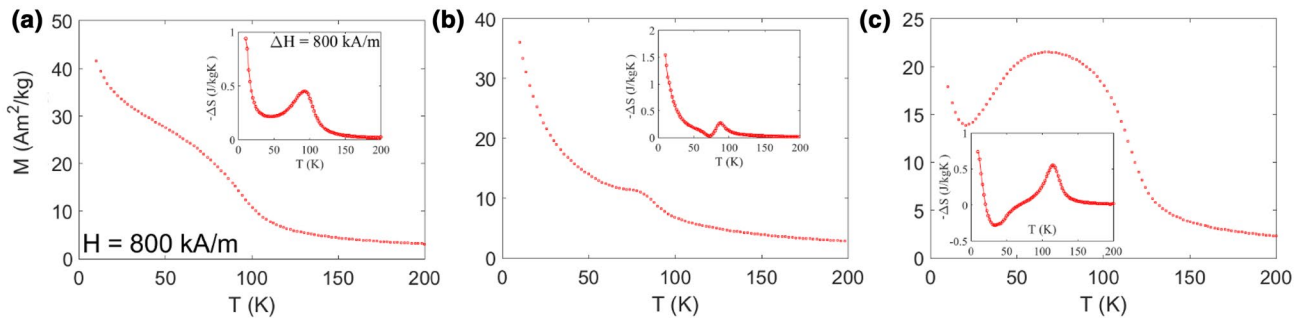


Fig. 8 Temperature dependence of the FC magnetization for **a** $\text{Dy}_2\text{NiMnO}_6$, **b** $\text{Dy}_2\text{CoMnO}_6$, and **c** $\text{Gd}_2\text{CoMnO}_6$, recorded in $H=800$ kA/m. The insets show the corresponding variation of the

magnetic entropy change estimated from the temperature derivative of the magnetization data (plotted as $-\Delta S$)

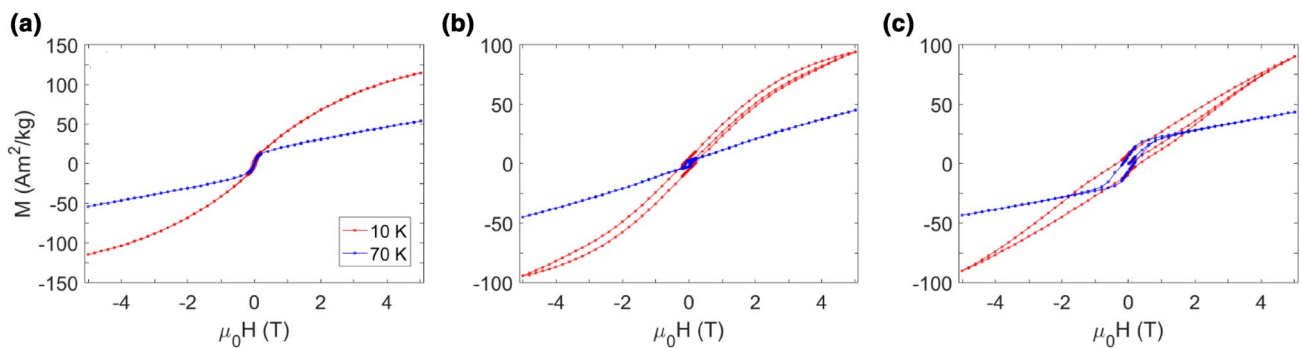


Fig. 9 Magnetization versus magnetic field, $M(H)$, curves recorded at $T=10$ K and 70 K for **a** $\text{Dy}_2\text{NiMnO}_6$, **b** $\text{Dy}_2\text{CoMnO}_6$, and **c** $\text{Gd}_2\text{CoMnO}_6$

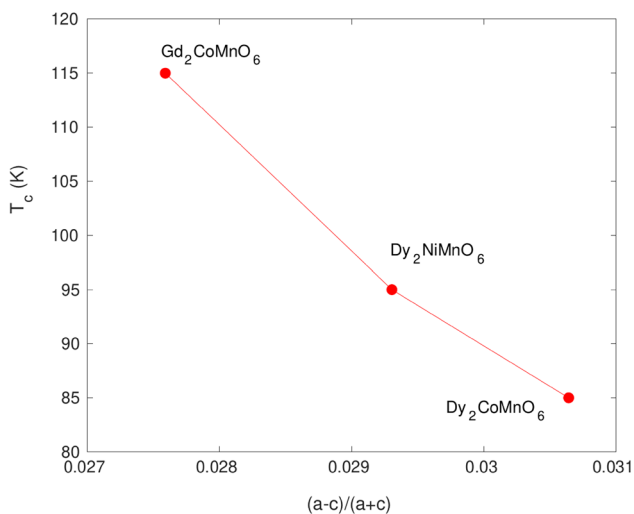


Fig. 10 Variation of T_C with the orthorhombic distortion $(a-c)/(a+c)$ calculated from the low-temperature XRPD data ($T=16$ K) refined in the $Pnma$ setting

of the coupling between the ordered 3d atoms and the large paramagnetic 4f moments in the three compounds.

5 Conclusions

The structural and magnetic properties of the ferrimagnetic double perovskites $\text{Dy}_2\text{CoMnO}_6$, $\text{Dy}_2\text{NiMnO}_6$ and $\text{Gd}_2\text{CoMnO}_6$ have been investigated. The crystal structure of the compounds was investigated as a function of temperature (16–1100 K). The materials adopt an orthorhombic structure with disordered Co(Ni)/Mn cations. The analysis of XRPD data shows that a clear change, although small, occurs in the BO_6 octahedron near T_C as evidenced by the $B-O-B$ bond angles and $B-O$ bond lengths. T_C was found to monotonously depend on the orthorhombic distortion of the compounds. The magnetic entropy changes were estimated from the temperature-dependent magnetization measurements for comparison of the magnetocaloric properties to those from literature. Contributions both from the ferrimagnetic transition and the 4f or 4f/3d magnetic moment interplay can be observed.

introduces substantial and complex magnetocaloric effects at low temperatures reflecting the different strength and sign

Acknowledgements Financial support for this work from the Russian Foundation for Basic Research (Grant 15-03-01676) and the Swedish Research Council is gratefully acknowledged.

Open Access This article is distributed under the terms of the Creative Commons Attribution 4.0 International License (<http://creativecommons.org/licenses/by/4.0/>), which permits unrestricted use, distribution, and reproduction in any medium, provided you give appropriate credit to the original author(s) and the source, provide a link to the Creative Commons license, and indicate if changes were made.

References

1. A. Hossain, P. Bandyopadhyay, S. Roy, An overview of double perovskites $A_2B'B''O_6$ with small ions at A site: synthesis, structure and magnetic properties. *J. Alloy. Compd.* **740**, 414–427 (2018)
2. S. Vasala, M. Karppinen, $A_2B'B''O_6$ perovskites: a review. *Prog. Solid State Chem.* **43**, 1–36 (2015)
3. Y. Shimakawa, M. Azuma, N. Ichikawa, Multiferroic compounds with double-Perovskite structures. *Materials* **4**, 153–168 (2011)
4. A.K. Kundu, *Magnetic Perovskites: Synthesis, Structure and Physical Properties*, (Springer, New York, 2016), p. 167
5. R.N. Mahato, K. Sethupathi, V. Sankaranarayanan, Colossal magnetoresistance in the double perovskite oxide La_2CoMnO_6 . *J. Appl. Phys.* **107**, 09D714–09D713 (2010)
6. D. Choudhury, P. Mandal, R. Mathieu, A. Hazarika, S. Rajan, A. Sundaresan, U.V. Waghmare, R. Knut, O. Karis, P. Nordblad, D.D. Sarma, Near-room-temperature colossal magnetodielectricity and multiglass properties in partially disordered La_2NiMnO_6 . *Phys. Rev. Lett.* **108**, 127201 (2012)
7. M.B. Jungfleisch, W. Zhang, A. Hoffmann, Perspectives of anti-ferromagnetic spintronics. *Phys. Lett. A* **382**, 865–871 (2018)
8. Y. Xu, M. Meier, P. Das, M. Koblishka, U. Hartmann, Perovskite manganites: potential materials for magnetic cooling at or near room temperature. *Cryst. Eng.* **5**, 383–389 (2002)
9. L. Mañosa, A. Planesa, M. Acet, Advanced materials for solid-state refrigeration. *J. Mater. Chem. A* **1**, 4925–4936 (2013)
10. K.A. Gschneidner Jr., V.K. Pecharsky, A.O. Tsoko, Recent developments in magnetocaloric materials. *Rep. Prog. Phys.* **68**, 1479–1539 (2005)
11. J. Krishna Murthy, K.D. Chandrasekhar, S. Mahana, D. Topwal, A. Venimadhav, Giant magnetocaloric effect in Gd_2NiMnO_6 and Gd_2CoMnO_6 ferromagnetic insulators. *J. Phys. D Appl. Phys.* **48**, 355001 (2015)
12. J. Krishna Murthy, A. Venimadhav, 4f-3d exchange coupling induced exchange bias and field induced Hopkinson peak effects in Gd_2CoMnO_6 . *J. Alloy. Compd.* **719**, 341–346 (2017)
13. L.S. Xu, L.L. Chen, J.Y. Fan, K. Bärner, L. Zhang, Y. Zhu, L. Pi, Y.H. Zhang, D.N. Shi, Room-temperature large magnetocaloric effect and critical behavior in $La_{0.6}Dy_{0.1}Sr_{0.3}MnO_3$. *Ceram. Int.* **42**, 8234–8239 (2016)
14. V. Franco, J.S. Blázquez, B. Ingale, A. Conde, The magnetocaloric effect and magnetic refrigeration near room temperature: materials and models. *Annu. Rev. Mater. Res.* **42**, 305–342 (2012)
15. M.-H. Phan, S.-C. Yu, Review of the magnetocaloric effect in manganite materials. *J. Magn. Magn. Mater.* **308**, 325–340 (2007)
16. N.S. Rogado, J. Li, A.W. Sleight, M.A. Subramanian, Magnetocapacitance and magnetoresistance near room temperature in a ferromagnetic semiconductor: La_2NiMnO_6 . *Adv. Mater.* **17**, 2225–2227 (2005)
17. J.Y. Moon, M.K. Kim, Y.J. Choi, N. Lee, Giant anisotropic magnetocaloric effect in double-perovskite Gd_2CoMnO_6 single crystals. *Scientific Reports* **7**, 16099 (2017)
18. Z.B. Guo, Y.W. Du, J.S. Zhu, H. Huang, W.P. Ding, D. Feng, Large magnetic entropy change in perovskite-type manganese oxides. *Phys. Rev. Lett.* **78**, 1142–1145 (1997)
19. W. Zhong, C.T. Au, Y.W. Du, Review of magnetocaloric effect in perovskite-type oxides. *Chin. Phys. B* **22**, 057501–057511 (2013)
20. Z.B. Guo, J.R. Zhang, H. Huang, W.P. Ding, Y.W. Du, Large magnetic entropy change in $La_{0.75}Ca_{0.25}MnO_3$. *Appl. Phys. Lett.* **70**, 904–905 (1997)
21. T. Raoufi, M.H. Ehsani, D.S. Khoshnoud, Magnetocaloric properties of $La_{0.6}Sr_{0.4}MnO_3$ prepared by solid state reaction method. *J. Alloy. Compd.* **689**, 865–873 (2016)
22. M.S. Anwar, F. Ahmed, B.H. Koo, Structural distortion effect on the magnetization and magnetocaloric effect in Pr modified $La_{0.65}Sr_{0.35}MnO_3$ manganite. *J. Alloy. Compd.* **617**, 893–898 (2014)
23. M. Khelifi, E. Dhahri, E.K. Hlil, Magnetic, magnetocaloric, magnetotransport and magnetoresistance properties of calcium deficient manganites $La_{0.8}Ca_{0.2-x}□_xMnO_3$ post-annealed at 800 °C. *J. Alloy. Compd.* **587**, 771–777 (2014)
24. N. Chau, P.Q. Niem, H.N. Nhat, N.H. Luong, N.D. Tho, Influence of Cu substitution for Mn on the structure, magnetic, magnetocaloric and magnetoresistance properties of $La_{0.7}Sr_{0.3}MnO_3$ perovskites. *Physica B* **327**, 214–2178 (2003)
25. T. Tang, K.M. Gu, Q.Q. Cao, D.H. Wang, S.Y. Zhang, Y.W. Du, Magnetocaloric properties of Ag-substituted perovskite-type manganites. *J. Magn. Magn. Mater.* **222**, 110–114 (2000)
26. P.L.C. Filho, P. Barrozo, D.A. Landinez-Tellez, R.F. Jardim, W.M. Azevedo, J. Albino Aguiar, structural and magnetic properties of Ln_2CoMnO_6 ($Ln = Dy$ and La) produced by combustion synthesis. *J. Supercond. Nov. Magn.* **26**, 2521–2524 (2013)
27. R.X. Silva, H. Reichlova, X. Marti, D.A.B. Barbosa, M.W. Lufaso, B.S. Araujo, A.P. Ayala, C. W. A. Paschoal spin-phonon coupling in $Gd(Co_{1/2}Mn_{1/2})O_3$ perovskite. *J. Appl. Phys.* **114**, 194102 (2013)
28. M.K. Kim, J.Y. Moon, H.Y. Choi, S.H. Oh, N. Lee, Y.J. Choi, Investigation of the magnetic properties in double perovskite R_2CoMnO_6 single crystals ($R =$ rare earth: La to Lu), *J. Phys. Condens. Matter* **27**, 426002 (2015)
29. A. Orayech, I. Urcelay-Olabarria, G.A. López, O. Fabelo, A. Faik, J.M. Igartua, Synthesis, structural, magnetic and phase transition studies of the ferromagnetic La_2CoMnO_6 double perovskite by symmetry-adapted modes. *Dalton Trans.* **44**, 13867–13880 (2015)
30. K. Mc Bride, N. Partridge, S. Bennington-Gray, S. Felton, L. Stella, D. Poulid, Synthesis, characterisation and study of magnetocaloric effects (enhanced and reduced) in manganate perovskites. *Mater. Res. Bull.* **88**, 69–77 (2017)
31. A.L. Li, L.G. Wang, X.X. Li, C.M. Zhu, R. Zhang, H.W. Wang, S.L. Yuan, Magnetic field-induced metamagnetism and magnetocaloric effect in double perovskites Re_2CoMnO_6 ($Re = Sm, Dy$). *Mater. Chem. Phys.* **202**, 76–81 (2017)
32. L. Su, X.-Q. Zhang, Q.-Y. Dong, Y.-J. Ke, K.-Y. Hou, C.-S. Liu, Z.-H. Cheng, Magnetocaloric effect and critical behaviors of R_2NiMnO_6 ($R = Eu$ and Dy) double perovskite oxides. *J. Alloys Compd.* **746**, 594–600 (2018)
33. T. Chakraborty, H. Nhalil, R. Yadav, A.A. Wagh, S. Elizabeth, Magnetocaloric properties of R_2NiMnO_6 ($R = Pr, Nd, Tb, Ho$, and Y) double perovskite family. *J. Magn. Magn. Mater.* **428**, 59–63 (2017)
34. M. Retuerto, Á Muñoz, M.J. Martínez-Lope, J.A. Alonso, F.J. Mompeán, M.T. Fernández-Díaz, J. Sánchez-Benítez, magnetic interactions in the double perovskites R_2NiMnO_6 ($R = Tb, Ho$,

- Er, Tm) investigated by neutron diffraction. *Inorg. Chem.* **54**, 10890–10900 (2015)
35. Y. Jia, Q. Wang, Y. Qi, L. Li, Multiple magnetic phase transitions and magnetocaloric effect in double perovskites R_2NiMnO_6 ($R = Dy, Ho,$ and Er). *J. Alloys Compd.* **726**, 1132–1137 (2017)
 36. A. Ganeshraj, R. Pradheesh, P.N. Santhosh, Structural, magnetic, transport and magnetocaloric properties of metamagnetic $DyMn_{0.5}Co_{0.5}O_3$. *J. Appl. Phys.* **111**, 07A914 (2012)
 37. K. Asai, K. Fujiyoshi, N. Nishimori, Y. Satoh, Y. Kobayashi, M. Mizoguchi, Magnetic properties of $REMe_{0.5}Mn_{0.5}O_3$ ($RE =$ Rare Earth Element, $Me = Ni, Co$). *J. Phys. Soc. Jpn.* **67**, 4218–4226 (1998)
 38. S. Chanda, S. Saha, A. Dutta, T.P. Sinha, Structural and transport properties of double perovskite Dy_2NiMnO_6 . *Mater. Res. Bull.* **62**, 153–160 (2015)
 39. H.Y. Zhou, X. M. Chen Structural distortions, orbital ordering and physical properties of double perovskite R_2CoMnO_6 calculated by first-principles. *J. Phys. Condens. Matter* **29**, 145701–145708 (2017)
 40. I.O. Troyanchuk, A.P. Sazonov, H. Szymczak, D.M. Töbrens, H. Gamari-Seale, Phase separation in $La_{2-x}A_xCoMnO_6$ ($A = Ca$ and Sr) perovskites. *J. Exp. Theo. Phys.* **99**, 2363–2369 (2004)
 41. M.G. Masud, K. Dey, A. Ghosh, S. Majumdar, S. Giri, Occurrence of magnetoelectric effect correlated to the Dy order in Dy_2NiMnO_6 double perovskite. *J. Appl. Phys.* **118**, 064104 (2015)
 42. Y. Jia, Q. Wang, P. Wang, L. Li, Structural, magnetic and magnetocaloric properties in R_2CoMnO_6 ($R = Dy, Ho,$ and Er). *Ceram. Int.* **43**, 15856–15861 (2017)
 43. I. Rodriguez-Carvajal, Recent advances in magnetic structure determination by neutron powder diffraction. *Physica B.* **192**, 55–69 (1993)
 44. M.P. Seah, Summary of ISO/TC 201 Standard: VII ISO 15472:2001—surface chemical analysis—X-ray photoelectron spectrometers—calibration of energy scales. *Surf. Interface Anal.* **31**, 721–723 (2001)
 45. P.E. Larson, M.A. Kelly, Surface charge neutralization of insulating samples in X-ray photoemission spectroscopy. *J. Vac. Sci. Technol. A* **16**, 3483–3489 (1998)
 46. M.W. Lufaso, P.W. Barnes, P.M. Woodward, Structure prediction of ordered and disordered multiple octahedral cation perovskites using SPuDS. *Acta Cryst. B* **62**, 397–410 (2006)
 47. G. King, P.M. Woodward, Cation ordering in perovskites. *J. Mater. Chem.* **20**, 5785–5796 (2010)
 48. I.B. Goodenough, An interpretation of the magnetic properties of the perovskite—type mixed crystal $La_{1-x}Sr_xCoO_{3-x}$. *J. Phys. Chem. Solids* **6**, 287–297 (1958)
 49. J. Kanamori, Superexchange interaction and symmetry properties of electron orbitals. *J. Phys. Chem. Solids* **10**, 87–98 (1959)
 50. I.D. Brown, VALENCE: a program for calculating bond valences. *J. Appl. Cryst.* **29**, 479–480 (1996)
 51. I.C. Biesinger, B.P. Payne, A.P. Grosvenor, L.W.M. Lau, A.R. Gerson, R. St. C. Smart, Resolving surface chemical states in XPS analysis of first row transition metals, oxides and hydroxides: Cr, Mn, Fe, Co and Ni. *Appl. Surf. Sci.* **257**, 2717–2730 (2011)
 52. R.J. Booth, R. Fillman, H. Whitaker, A. Nag, R.M. Tiwari, K. Ramanujachary, J. Gopalakrishnan, S.E. Lofland, An investigation of structural, magnetic and dielectric properties of R_2NiMnO_6 ($R =$ rare earth, Y). *Mater. Res. Bull.* **44**, 1559 (2009)
 53. M. Hudl, R. Mathieu, P. Nordblad, S.A. Ivanov, G.V. Bazuev, P. Lazor, Investigation of the magnetic phase transition and magnetocaloric properties of the Mn_2FeSbO_6 ilmenite. *J. Magn. Magn. Mater.* **331**, 193–197 (2013)
 54. X. Bohigas, J. Tejada, E. del Barco, X.X. Zhang, M. Sales tunable magnetocaloric effect in ceramic perovskites. *Appl. Phys. Lett.* **73**, 390–392 (1998)
 55. R. Galceran, C. Frontera, L. Balcells, J. Cisneros-Fernández, L. López-Mir, J. Roqueta, J. Santiso, N. Bagués, B. Bozzo, A. Pomar, F. Sandiumenge, B. Martínez, Engineering the microstructure and magnetism of $La_2CoMnO_{6-\delta}$ thin films by tailoring oxygen stoichiometry. *Appl. Phys. Lett.* **105**, 242401–242404 (2014)
 56. L.Y. Wang, Q. Li, Y.Y. Gong, D.H. Wang, Q.Q. Cao, Y.W. Du, The positive and negative magnetodielectric effects in double perovskite Pr_2CoMnO_6 . *J. Am. Ceram. Soc.* **97**, 2024–2026 (2014)
 57. A.J. Barón-González, C. Frontera, J.L. García-Muñoz, B. Rivas-Murias, J. Blasco, Effect of cation disorder on structural, magnetic and dielectric properties of La_2MnCoO_6 double perovskite. *J. Phys. Condens. Matter.* **23**, 496003–496014 (2011)
 58. A.N. Sayed, S.N. Achary, S.K. Deshpande, B. Rajeswari, R.M. Kadam, S. Dwebedi, A.K. Nigam, A. K. Tyagi, Role of annealing atmosphere on structure, dielectric and magnetic properties of La_2CoMnO_6 and La_2MgMnO_6 . *Z. Anorg. Allg. Chem.* **640**, 1907–1921 (2014)
 59. I.T. Anderson, K.B. Greenwood, G.A. Taylor, K.R. Poeppelmeier, B-cation arrangements in double perovskites. *Prog. Solid State Chem.* **22**, 3197–3233 (1993)